

GALAXY SURFACE PHOTOMETRY

Bo Milvang-Jensen^{1,2} and Inger Jørgensen³

¹ *Copenhagen University Observatory, 2100 Copenhagen Ø, Denmark, milvang@astro.ku.dk*

² *School of Physics and Astronomy, University of Nottingham, University Park, NG7 2RD Nottingham, UK (postal address for BMJ)*

³ *Gemini Observatory, 670 N. Aohoku Pl., Hilo, Hawaii 96720, USA, ijorgensen@gemini.edu*

Received March 3, 2000

Abstract. We describe galaxy surface photometry based on fitting ellipses to the isophotes of the galaxies. Example galaxies with different isophotal shapes are used to illustrate the process, including how the deviations from elliptical isophotes are quantified using Fourier expansions. We show how the definitions of the Fourier coefficients employed by different authors are linked. As examples of applications of surface photometry we discuss the determination of the relative disk luminosities and the inclinations for E and S0 galaxies. We also describe the color-magnitude and color-color relations. When using both near-infrared and optical photometry, the age-metallicity degeneracy may be broken. Finally we discuss the Fundamental Plane where surface photometry is combined with spectroscopy. It is shown how the FP can be used as a sensitive tool to study galaxy evolution.

Key words: techniques: photometric – galaxies: photometry – galaxies: fundamental parameters – galaxies: elliptical and lenticular, cD – galaxies: stellar content – galaxies: evolution

1. INTRODUCTION

Surface photometry of galaxies is a technique to quantitatively describe the light distribution of the galaxies, as recorded in 2-dimensional images. This paper focuses on the techniques used to

derive the surface photometry and presents some examples of scientific applications. The paper is a summary of the lectures given at the summer school, and is not intended as a complete review of the topic. Surface photometry of galaxies has previously been reviewed by Kormendy & Djorgovski (1989) and Okamura (1988).

The techniques and the software used for performing surface photometry of galaxies are described in Section 2. Surface photometry has many applications. In Section 3 we give an example of such an application, namely the determination of disk luminosities and inclinations of E and S0 galaxies. This determination is based on surface photometry – ellipticities and deviations from elliptical shape – alone.

From surface photometry in several passbands we can derive the colors of the galaxies. These colors provide information about the ages and the metal content of the stellar populations in the galaxies. In order to study this, stellar population models are needed. These models are the subject of Section 4. In Section 5, we then present examples of the color-magnitude and color-color relations of galaxies.

Although the topic of this summer school is photometry, we will nevertheless show an example of the science that can be carried out when surface photometry is combined with spectroscopy. The chosen example is the relation known as the Fundamental Plane for E and S0 galaxies, which we discuss in Section 6.

We end this description of surface photometry with a few suggestions for future projects that can be carried out based on surface photometry only, see Section 7.

Throughout the paper we use $H_0 = 50 \text{ km s}^{-1} \text{ Mpc}^{-1}$.

2. SURFACE PHOTOMETRY

Surface photometry is used to study *extended objects*, such as galaxies, as opposed to *point sources*, such as stars. From an image of a point source, only its total magnitude can be derived. From an image of a galaxy, it is possible to determine a number of quantities. Some of these quantities are derived from surface photometry, such as how the intensity and ellipticity vary with radius. Other quantities are determined by other methods – the morphological type, for example, is determined from visual inspection of the image. There also exist schemes to do automated morphological classification, e.g. Abraham et al. (1994, 1996); Naim et al. (1995).

In this context, we are talking about galaxies where the individual stars cannot be resolved in the images. This is for example the case for the HydraI (Abell 1060) cluster, which is a nearby cluster at a distance of ~ 80 Mpc. At that distance, even the Hubble Space Telescope (HST) cannot resolve individual stars in the galaxies.

Photometry of crowded stellar fields, such as globular clusters, is not considered surface photometry. Surface photometry is used when the magnitudes of the individual stars (typically in a galaxy) cannot be measured, but only their smooth integrated light.

2.1 Ellipse fitting

Surface photometry of galaxies is usually done by fitting ellipses to the isophotes. This choice is motivated by that fact that the isophotes of galaxies are not far from ellipses. This is especially the case for elliptical (E) and lenticular (S0) galaxies. In this paper we will concentrate on E and S0 galaxies. We will also limit our discussion to data obtained with CCDs (Charge-Coupled Devices).

There exist several software packages for deriving surface photometry. For the exercise related to the lectures given at the summer school we have chosen the ELLIPSE task in the ISOPHOTE package (see Busko 1996). This task is based on the ellipse fitting algorithm used in the GASP package by Cawson (1983; see also Davis et al. 1985), the code for which was later rewritten by Jedrzejewski (1987). ISOPHOTE is a part of the external IRAF* package STSDAS**. We chose this software for the exercise since it is publicly available, and because it includes some documentation. The examples of surface photometry presented in this section are also based on the ISOPHOTE package. Our aim is to describe the basic principles of surface photometry based on ellipse fitting, and the choice of software package is not critical for that purpose. A comparison of the results obtained with ELLIPSE with those obtained with other software packages is beyond the scope of this paper.

* IRAF is distributed by the National Optical Astronomy Observatories, which are operated by the Association of Universities for Research in Astronomy, Inc., under cooperative agreement with the National Science Foundation. See also <http://iraf.noao.edu/>

** STSDAS is distributed by the Space Telescope Science Institute, operated by AURA, Inc., under NASA contract NAS 5-26555. See also <http://ra.stsci.edu/STSDAS.html>

To illustrate how surface photometry on E and S0 galaxies is derived we have chosen three example galaxies, see Figure 1 and Table 1. We will refer to these galaxies as the ‘pure E’, the ‘S0’ and the ‘boxy E’, respectively. The name ‘pure E’ refers to the fact that the isophotes of this galaxy are almost perfect ellipses. For the ‘boxy E’, the isophotes are box shaped. The pure E has been morphologically classified as E3/S0. The boxy E has been morphologically classified as SB(rs)0(0) (barred S0 with rings). For our purpose of illustrating surface photometry these morphological types are not important.

Table 1. The three example galaxies

Description	Name	Morph. type	M_{rT}	r_{e}
Pure E	R347 / IC2597	E3/S0	−23.35 mag	8.9 kpc
S0	R338	S0(5)	−20.74 mag	1.9 kpc
Boxy E	R245	SB(rs)0(0)	−20.94 mag	4.8 kpc

Note: Name and morphological type are from Richter (1989). Total absolute Gunn r magnitude (M_{rT}) and effective radius (r_{e}) are from Milvang-Jensen & Jørgensen (2000), based on $H_0 = 50 \text{ km s}^{-1} \text{ Mpc}^{-1}$.

The example galaxies are all members of the HydraI (Abell 1060) cluster. The images used are 300 sec Gunn r exposures ($\lambda_{\text{eff}} = 6550 \text{ Å}$, Thuan & Gunn 1976) obtained with the Danish 1.5-meter Telescope, La Silla, Chile. The spatial scales, as well as the grey-scales of the images of the three galaxies in the figures are identical, allowing a direct visual comparison between the three galaxies. The intensity scaling in the images shown on Figure 1 is logarithmic. We have given lengths in kpc rather than arcsec. To calculate lengths in arcsec, use $\log(\ell/\text{arcsec}) = \log(\ell/\text{kpc}) + 0.407$. The corresponding distance modulus for the cluster is $(m - M) = 34.60 \text{ mag}$.

In doing the surface photometry, the first step is to identify the other objects in the image (other galaxies, stars, and cosmic ray events) and mask (flag) these. This is shown in Figure 2. The masked pixels are not used in the surface photometry of the galaxy. The masking shown in Figure 2 uses squares for the masking of objects. A masking using circles is of course also possible, and that would mask fewer ‘uncontaminated’ pixels.

Once the masking is done, we need only provide the surface photometry task the approximate location of the center of the galaxy.

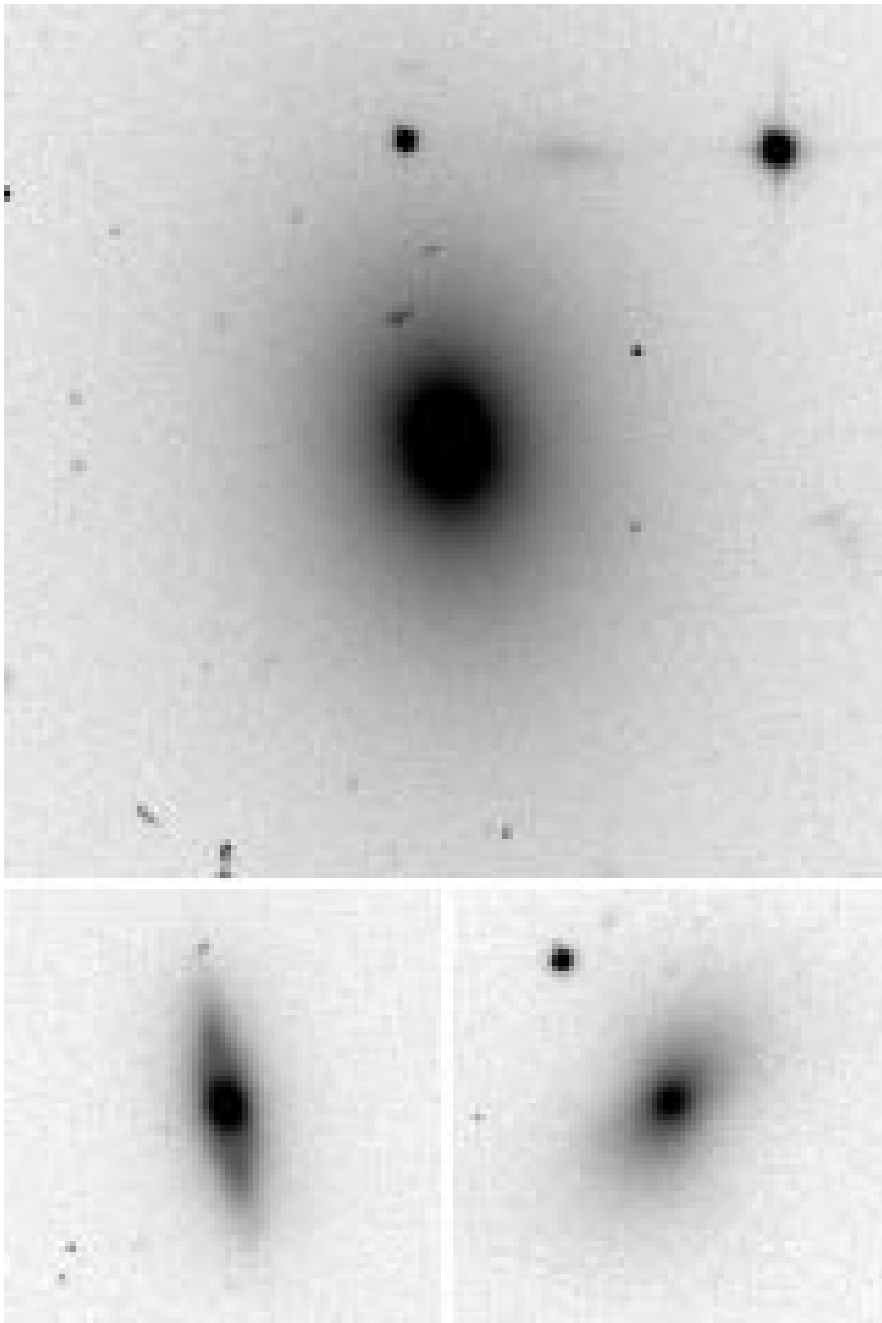


Fig. 1. The three example galaxies – pure E (top), S0 (left), boxy E (right). The width of the montage is 32 kpc. North is down and east is to the right.

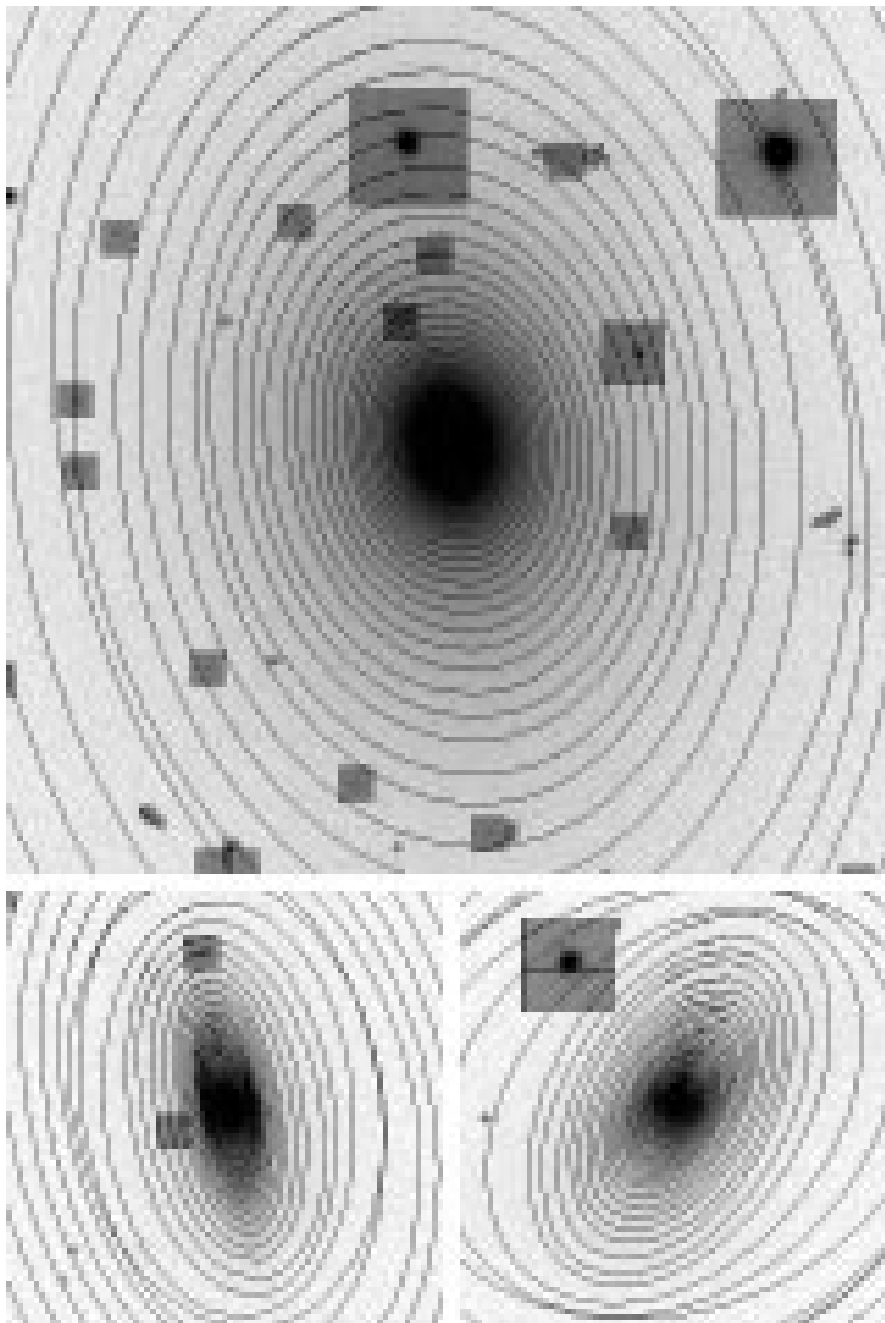


Fig. 2. The three example galaxies, with best-fitting ellipses, and with pixels contaminated by other objects flagged (the hatched areas).

The task then fits ellipses to the intensities in the image. This is done at a number of discrete radii, as also shown in Figure 2. For the ELLIPSE task, these discrete radii are specified by the rule that the different semi-major axis lengths a are spaced by a factor of 1.1.

The center (x, y) and the shape (ellipticity ϵ and position angle) of the ellipses are kept as free parameters in the fit for semi-major axes at which the signal-to-noise ratio is sufficiently high. For larger semi-major axes, where the signal-to-noise ratio is lower, the center and shape of the ellipses are fixed.

We get two types of output from the ellipse fit. One type is the residual image, which is the difference between the original image and the model image based on the best-fitting ellipses. The residual images for the three example galaxies are shown in Figure 3.

For the pure E, the residuals are fairly small. For the S0 in particular, and for the boxy E, the residuals are larger. The pure E is much brighter than the other two galaxies, so in relative terms the residuals for the pure E are much smaller than for the other two galaxies. For the pure E, very little structure is seen in the residual image. The residual images of the S0 and the boxy E show clear structures. In Section 2.2 we will discuss how to quantify these structures.

The other type of output from the ellipse fit is the *radial profiles* of a number of quantities. I.e., for each ellipse we get the intensity, center, ellipticity, position angle, and measures of the deviations from perfect elliptical isophotes (see Section 2.2), as well as the uncertainties for all these quantities. In Figure 4 we show the radial profiles of intensity, ellipticity and position angle for the three example galaxies. The position angles shown in Figure 4 are measured counter-clockwise from the y -axis of the images. The ELLIPSE task adopts this definition of position angles. The standard (astronomical) definition of position angles is from north through east. Our images have north down and east to the right, and thus need to be rotated by 180° to have the y -axis pointing towards north. However, position angles are only unique to within 180° since the major axis of a galaxy does not have a direction (as opposed to a coordinate axis). Therefore, the position angles shown in Figure 4 are expressed in the standard way. It also follows, for example, that the position angle of the inner isophotes of the boxy galaxy could be said to be 150° as well as -30° .

In Figure 4, we have plotted the different quantities against the logarithm of the *equivalent radius* r . The equivalent radius is defined

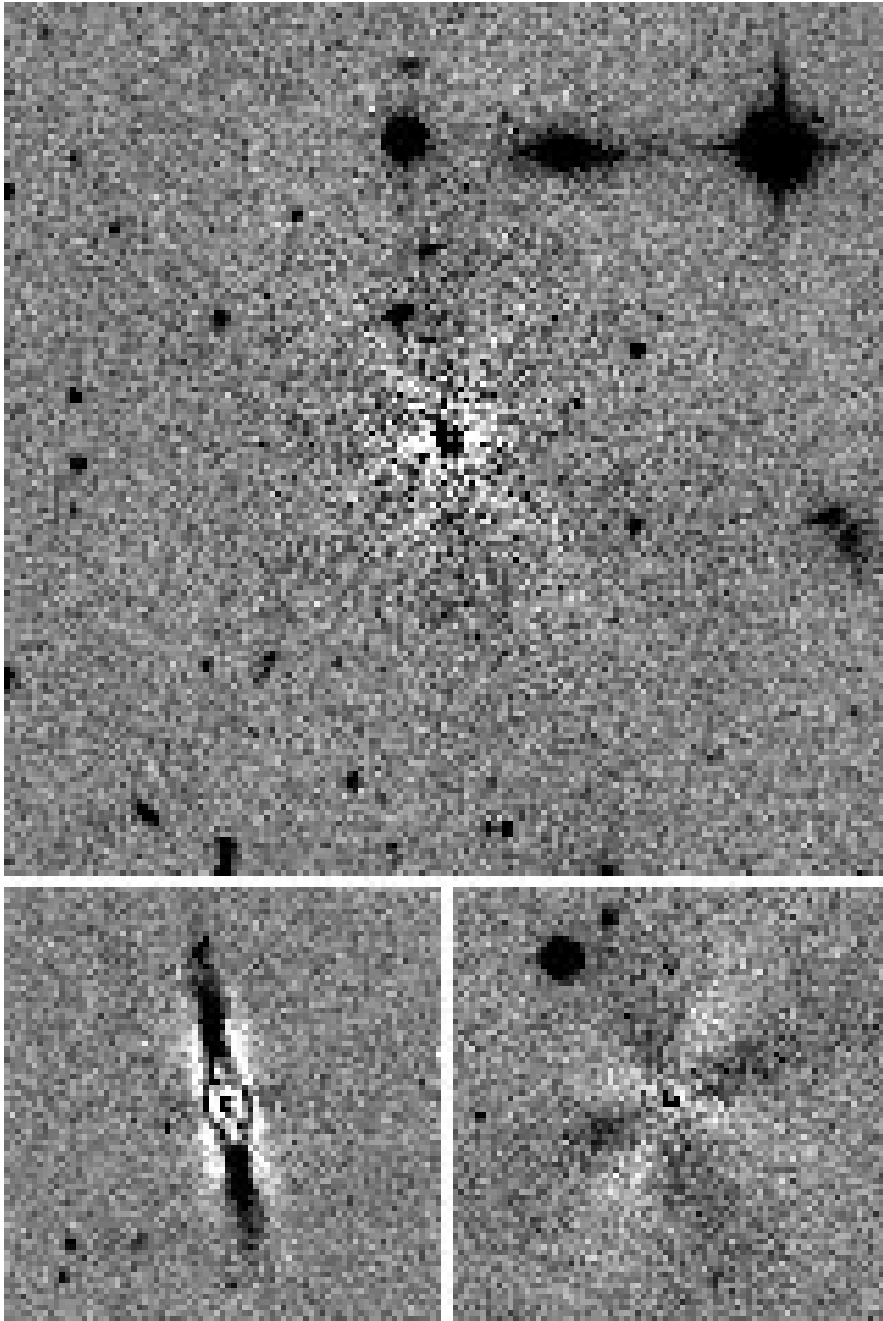


Fig. 3. The three example galaxies: residual images (i.e. the original image minus the model image). The intensity scaling is linear, and the cuts are symmetrical around zero. Black represents positive residuals.

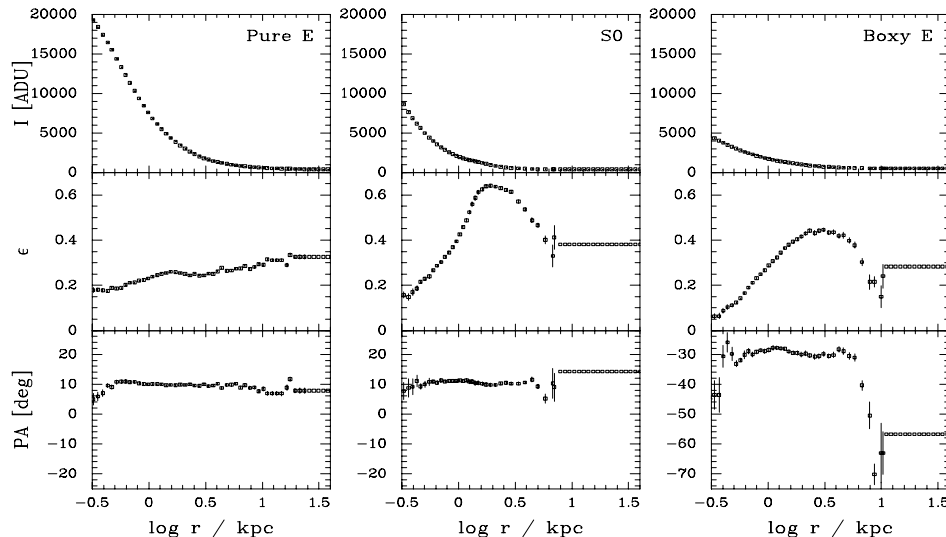


Fig. 4. Radial profiles of intensity, ellipticity and position angle for the three example galaxies. The plotted range in equivalent radii r is 0.3–40 kpc ($0.8''$ – $102''$).

by $r = \sqrt{ab}$, where a and b are the semi-major and semi-minor axis of the ellipse, respectively. A circle with radius r has an area equivalent to an ellipse with axes a and b , hence the name *equivalent* radius. The program used for the illustrations in this section, ELLIPSE, uses a to characterize the size of the ellipses. However, since the ellipticity ϵ of the ellipse is defined as $\epsilon = 1 - b/a$, it follows that r can be calculated from a and ϵ as $r = a\sqrt{1 - \epsilon}$.

From Figure 4 it is seen how the ellipticity and position angle are free parameters until a certain radius where their values are fixed. The ellipticity is seen to vary with radius for all three galaxies. The position angle for the boxy galaxy is seen to vary rapidly in the outer parts, which is also seen in Figure 2. This behavior is known as an isophote twist.

2.2 Quantifying the deviations from elliptical shapes

As we saw from the residual images in Figure 3, the isophotes of E and S0 galaxies are not always perfectly elliptical. We wish to quantify these deviations from elliptical shapes. To illustrate how this is done, we have chosen an *example ellipse* for each of the three example galaxies. The three example ellipses are shown in Figure 5,

6 and 7 – they are overlayed both on the original and on the residual images of the example galaxies.

In Figure 5, 6 and 7, we also plot the quantity

$$\Delta I_{\text{norm}} \equiv \frac{I - I_0}{r \cdot \left| \frac{dI}{dr} \right|} . \quad (1)$$

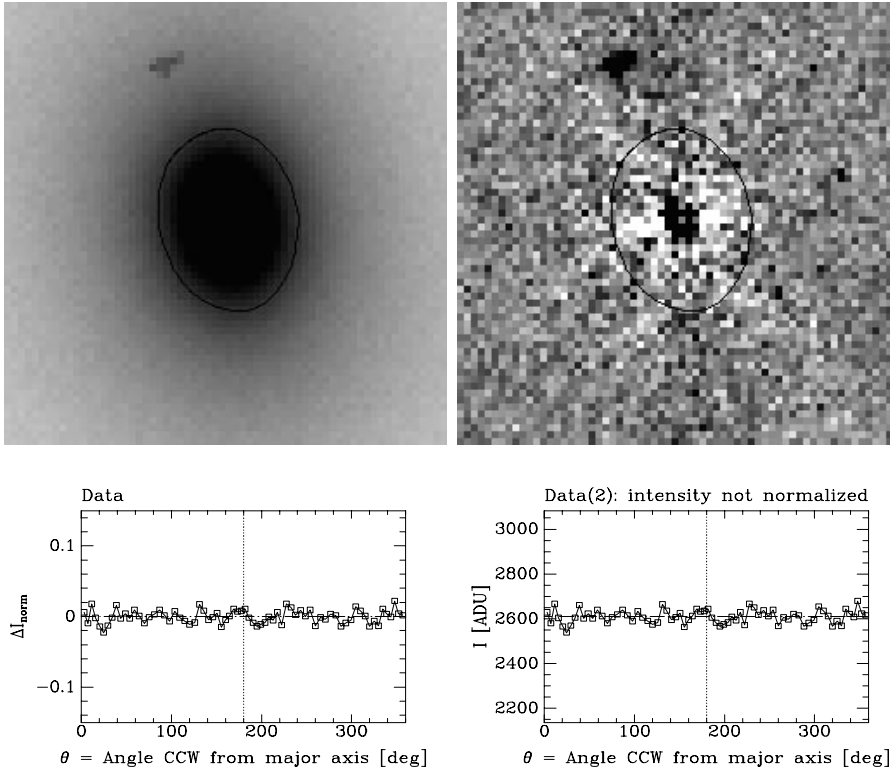


Fig. 5. Top: Original and residual images of the pure E galaxy, with a single ellipse at $a = 2.6$ kpc ($r = 2.3$ kpc) shown. The images are 13 kpc on the side. The ‘Data’ plot shows ΔI_{norm} versus θ (see text) along the shown ellipse. The ‘Data(2)’ plot shows the same, except that the intensity I is used rather than ΔI_{norm} . Little structure is seen, consistent with the fact that all the Fourier coefficients are close to zero, see Table 2.

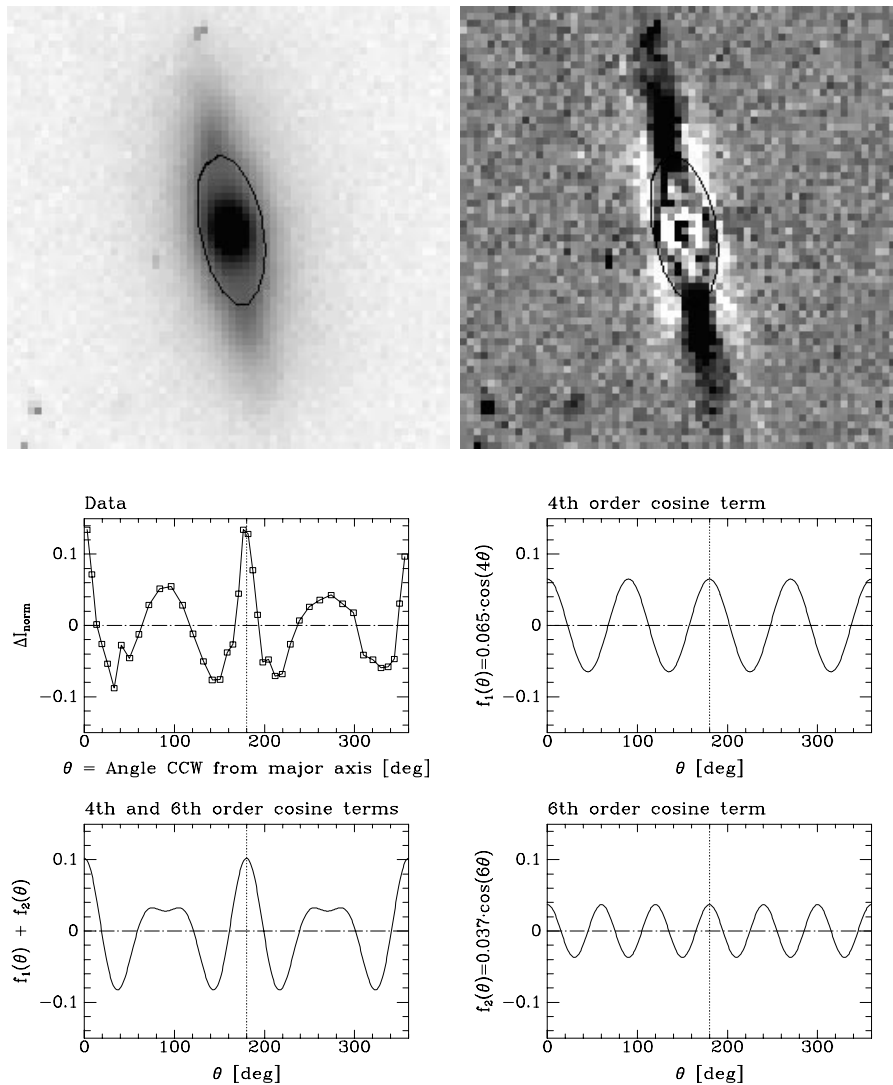


Fig. 6. Top: Original and residual images of the S0 galaxy, with a single ellipse at $a = 2.2$ kpc ($r = 1.4$ kpc) shown. The images are 13 kpc on the side. The ‘Data’ plot shows ΔI_{norm} versus θ along the shown ellipse. Substantial structure is seen. The starting point of the curve ($\theta = 0^\circ$) corresponds to the apogee of the ellipse that is closest to the top of the figure. At that point the residual is positive (black). The angle θ is measured counter-clockwise. The two most dominant Fourier modes, the 4th and 6th order cosine terms, cf. Table 2, are illustrated in the three other plots. This example galaxy is a disk galaxy and as such has a positive c_4 (4th order cosine coefficient).

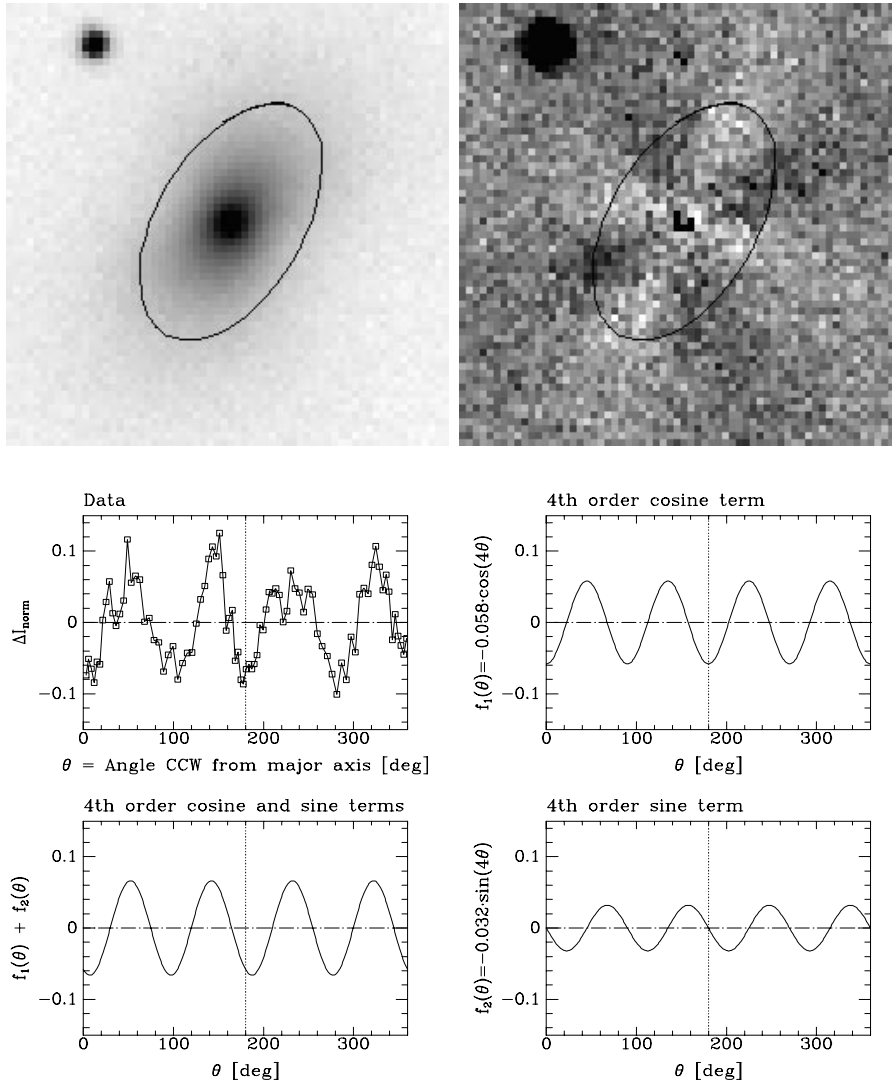


Fig. 7. Top: Original and residual images of the boxy galaxy, with a single ellipse at $a = 3.8$ kpc ($r = 2.8$ kpc) shown. The images are 13 kpc on the side. The ‘Data’ plot shows ΔI_{norm} versus θ along the shown ellipse. Substantial structure is seen. The starting point of the curve ($\theta = 0^\circ$) corresponds to the apogee of the ellipse that is closest to the top of the figure. At that point the residual is negative (white). The angle θ is measured counter-clockwise. The two most dominant Fourier modes, the 4th order cosine and sine terms, cf. Table 2, are illustrated in the three other plots. Note how a boxy galaxy has a negative c_4 (4th order cosine coefficient).

As can be seen, ΔI_{norm} is the deviation in intensity I from the mean intensity at the given ellipse, I_0 , normalized by the equivalent radius r , and by the absolute value of the intensity gradient, $|dI/dr|$. For comparison, we also show the intensity I in Figure 5. The reason for choosing this particular normalization will be described in the following. One advantage of using the quantity ΔI_{norm} in the plots is that allows a direct comparison between the plots for the three example galaxies.

To quantify how the *intensity* deviates from being constant along the fitted ellipse, the following Fourier series is fitted to the intensity $I(\theta)$

$$I(\theta) = I_0 + \sum_{n=1}^N [A_n \sin(n\theta) + B_n \cos(n\theta)] \quad . \quad (2)$$

N is the highest order fitted. θ is the angle measured counter-clockwise from the major axis of the ellipse. The different Fourier modes, e.g. $\cos 4\theta$, will be discussed below.

We are more interested in how the *isophote* deviates (in the radial direction) from the fitted ellipse. Let $R_{\text{iso}}(\theta)$ denote the distance from the center of the ellipse to the isophote, and let $R_{\text{ell}}(\theta)$ denote the distance from the center of the ellipse to the ellipse itself. For a perfectly elliptical isophote, the difference between $R_{\text{iso}}(\theta)$ and $R_{\text{ell}}(\theta)$ would be zero for all values of θ . We can Fourier expand the difference as

$$\Delta R(\theta) \equiv R_{\text{iso}}(\theta) - R_{\text{ell}}(\theta) = \sum_{n=1}^N [A'_n \sin(n\theta) + B'_n \cos(n\theta)] \quad . \quad (3)$$

$\Delta R(\theta)$ is the radial deviation of the isophote from elliptical shape. The *relative* deviation is more interesting, so we take $\Delta R(\theta)$ relative to the size of the ellipse, given by the equivalent radius r . This relative radial deviation of the isophote from elliptical shape, $\Delta R(\theta)/r$, is described by the Fourier coefficients A'_n/r and B'_n/r . We will allocate new symbols for these quantities: $s_n \equiv A'_n/r$ and $c_n \equiv B'_n/r$.

The ELLIPSE task calculates A_n and B_n , but not A'_n and B'_n . However, we are able to link the two sets of coefficients. Consider a Taylor expansion to first order of $I(R)$ around R_0

$$I(R) = I(R_0) + \frac{dI}{dR}(R - R_0) \quad . \quad (4)$$

Let R be a point on the isophote and let R_0 be a point on the ellipse. $I(R)$ is constant since R is on the isophote. The intensity on the ellipse $I(R_0)$ is not necessarily constant. The intensity on the ellipse is also given by $I(\theta)$ (Equation 2). We can identify the difference $(R - R_0)$ with $\Delta R(\theta)$ (Equation 3). A suitable mean value of the gradient dI/dR is dI/dr . (The ‘effective intensity gradient’ dI/dr can be calculated as the difference in intensity divided by the difference in equivalent radius for two adjacent ellipses.) By inserting Equation (2) and (3) in Equation (4) we find the following relations hold for all n

$$A'_n = \frac{A_n}{\left|\frac{dI}{dr}\right|} , \quad B'_n = \frac{B_n}{\left|\frac{dI}{dr}\right|} , \quad (5)$$

where we have used $-dI/dr = |dI/dr|$ since the intensity gradient is negative. From the definitions of s_n and c_n given above, we finally get

$$s_n = \frac{A_n}{r \cdot \left|\frac{dI}{dr}\right|} , \quad c_n = \frac{B_n}{r \cdot \left|\frac{dI}{dr}\right|} . \quad (6)$$

These definitions of the Fourier coefficients s_n and c_n are used in the literature by e.g. Franx, Illingworth & Heckman (1989b); Jørgensen, Franx & Kjørgaard (1992); Jørgensen & Franx (1994); and Jørgensen, Franx & Kjørgaard (1995).

Slightly different definitions are also in use. Some authors, e.g. Bender & Möllenhoff (1987); Bender, Döbereiner & Möllenhoff (1988); Bender et al. (1989); and Nieto & Bender (1989), use a_4/a for the 4th order cosine coefficient (still for the radial deviation). In our notation, this is equal to B'_4/a . The only difference between c_4 and a_4/a is that $c_4 \equiv B'_4/r$ is taken relative to the equivalent radius r , whereas $a_4/a = B'_4/a$ is taken relative to the semi-major axis a . Thus, the two are related by

$$a_4/a = c_4 r/a = c_4 \sqrt{1 - \epsilon} = c_4 \sqrt{b/a} , \quad (7)$$

where we have used the known relations between r , a , b and ϵ . For an apparently round galaxy (i.e. for $\epsilon = 0$), a_4/a is equal to c_4 .

Yet another definition is used by e.g. Peletier et al. (1990). These authors expand the intensity along the ellipse as

$$I(\theta) = I_0 \left(1 + \sum_{n=1}^N [S_n \sin(n\theta) + C_n \cos(n\theta)] \right) \quad (8)$$

(note the upper case C_n). When comparing with Equation (2) it is seen that $I_0 S_n = A_n$ and $I_0 C_n = B_n$. This means, for example, that c_4 and C_4 are related as

$$C_4 = c_4 \frac{r}{I_0} \cdot \left| \frac{dI}{dr} \right| = c_4 \cdot \left| \frac{d \log I}{d \log r} \right|. \quad (9)$$

It also follows that a_4/a is related to C_4 by

$$a_4/a = C_4 \cdot \left| \frac{d \log I}{d \log r} \right|^{-1} \sqrt{b/a}, \quad (10)$$

a relation used by Faber et al. (1997) (but note the upper case C_4).

Table 2. Fourier coefficients for the three example galaxies at the particular ellipses shown in Figure 5, 6 and 7. The semi-major axis a for these ellipses is given.

Coeff.	pure E $a = 2.6$ kpc	S0 $a = 2.2$ kpc	boxy E $a = 3.8$ kpc
c_3	0.001 ± 0.002	-0.003 ± 0.013	0.002 ± 0.008
s_3	-0.001 ± 0.002	-0.000 ± 0.014	-0.002 ± 0.008
c_4	0.000 ± 0.002	0.065 ± 0.013	-0.058 ± 0.006
s_4	-0.004 ± 0.002	0.001 ± 0.008	-0.032 ± 0.005
c_5	0.000 ± 0.002	-0.003 ± 0.008	0.002 ± 0.004
s_5	0.001 ± 0.002	0.007 ± 0.008	-0.006 ± 0.004
c_6	0.003 ± 0.001	0.037 ± 0.006	-0.018 ± 0.004
s_6	-0.002 ± 0.001	-0.000 ± 0.006	0.012 ± 0.004
c_7	-0.000 ± 0.001	-0.001 ± 0.006	0.010 ± 0.003
s_7	-0.002 ± 0.001	-0.000 ± 0.006	-0.005 ± 0.003
c_8	0.004 ± 0.001	0.021 ± 0.005	-0.004 ± 0.003
s_8	-0.001 ± 0.001	0.003 ± 0.005	0.005 ± 0.003

The fitted values of the Fourier coefficients c_n and s_n for the example ellipses for the three example galaxies are listed in Table 2. For the S0 galaxy, it is seen that the two numerically largest coefficients are $c_4 = 0.065$ and $c_6 = 0.037$. For the boxy galaxy the two numerically largest coefficients are $c_4 = -0.058$ and $s_4 = -0.032$.

From the definition of ΔI_{norm} (Equation 1), and from Equation (3) and (4) it is seen that $\Delta I_{\text{norm}} = \Delta R(\theta)/r$, i.e. ΔI_{norm} measures

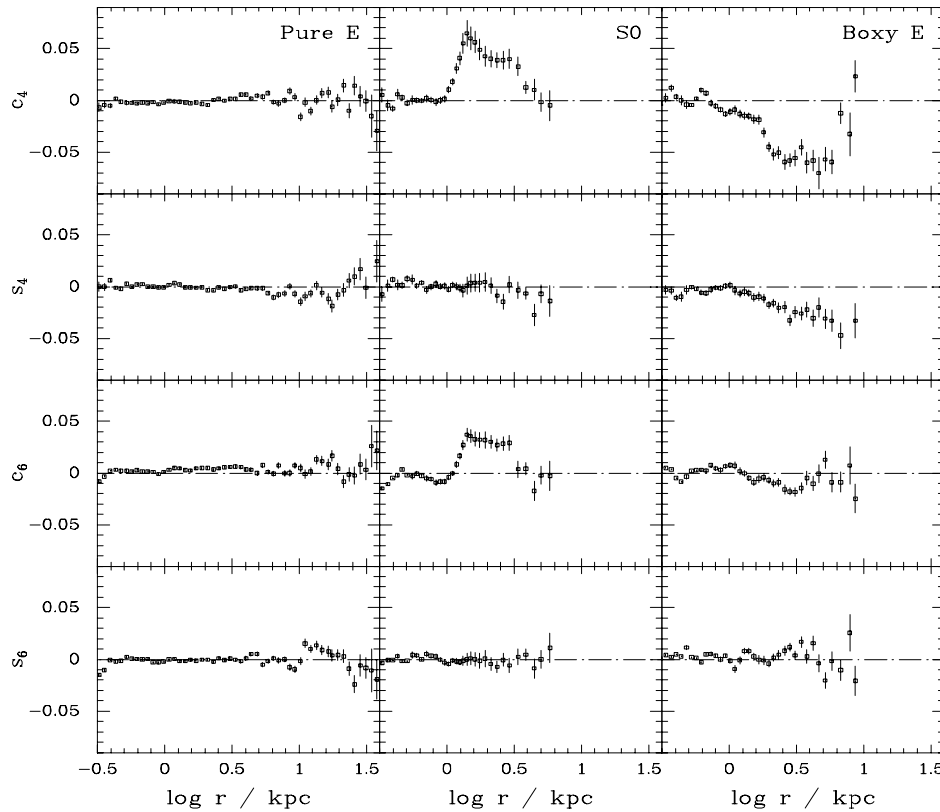


Fig. 8. Radial profiles of the Fourier coefficients c_4 , s_4 , c_6 and s_6 for the three example galaxies. The plotted range in equivalent radii r is 0.3–40 kpc ($0.8''$ – $102''$). Points with uncertainty larger than 0.025 are not plotted.

the relative radial deviation of the isophote from elliptical shape. This is also the quantity measured by s_n and c_n (indeed, they are the Fourier coefficients of $\Delta R(\theta)/r$), so plots of the Fourier modes $s_n \sin(n\theta)$ and $c_n \cos(n\theta)$ can be directly compared with the ΔI_{norm} versus θ plot. In Figure 6 and 7 we show the two most important Fourier modes and their sum for the S0 galaxy and the boxy E galaxy, respectively. It is seen in both cases how the two most important modes account for most of the structure.

An ellipse can be described by the first and second order Fourier coefficients. Since the Fourier expansion is along the best-fitting ellipses, the first and second order Fourier coefficients obtained there will be zero.

The cosine modes are symmetrical around the major axis ($\theta = 0^\circ$ or 180°), whereas the sine modes are not, see Figure 7. The odd cosine modes (e.g. 3rd order) are not symmetrical around the *minor* axis (see Figure 1a in Peletier et al. 1990). The mode that is dominating for most E and S0 galaxies is the 4th order cosine. Note from Figure 6 and 7 how c_4 is an indicator of disk ($c_4 > 0$) or boxy ($c_4 < 0$) isophotes aligned with the major axis (e.g. Carter 1987; Bender et al. 1989; Peletier et al. 1990).

The radial profiles of the 4th and 6th order Fourier coefficients are shown in Figure 8.

2.2.1 The output from the ELLIPSE task

The radial profiles determined by the ELLIPSE task are output to an STSDAS table. The most important columns are listed in Table 3, along with their meaning in our notation.

The equivalent radius is not in the table, but it can be calculated as `SMA*sqrt(1-ELLIP)`. The 5th to 8th order Fourier coefficients s_n and c_n can be calculated as e.g. $c_6 = \text{BI6}/(\text{SMA}*\text{abs}(\text{GRAD}))$. This follows from Equation (6) since $a \, dI/da = r \, dI/dr$. Note that the GRAD column is dI/da (I. Busko 2000, private communication).

Table 3. Output columns from ELLIPSE

Column name	Content in our notation
SMA	a
INTENS	I
ELLIP	ϵ
PA	PA (position angle)
X0	x (center of ellipse)
Y0	y (center of ellipse)
GRAD	dI/da (not dI/dr)
An	$s_n, n = 3, 4$
Bn	$c_n, n = 3, 4$
AIn	$A_n, n = 5, 6, 7, 8^a$
$BI n$	$B_n, n = 5, 6, 7, 8^a$

^a Only calculated with the following option set:
`harmonics="5 6 7 8"`.

2.3 Determination of magnitudes

The intensity I (in ADU) contains the signal from the galaxy plus the sky background. The sky background level can be determined in several ways. One way is to identify *empty regions* in the image and measure the level there. If the galaxy fills most of the image, this can be difficult. Another way is to fit a suitable analytical expression to outer part of galaxy plus sky intensity profile obtained from the surface photometry. This method has been used by e.g. Jørgensen et al. (1992), fitting $I_{\text{galaxy+sky}}(r) = I_{\text{sky}} + I_{\text{galaxy},0} \cdot r^{-\alpha}$, with $\alpha = 2$ or 3 .

Magnitudes can be calculated from the sky subtracted intensity. This can either be integrated magnitudes within a certain aperture (elliptical or circular), or the surface brightness at a given ellipse, $\mu(r)$. By knowing the pixel scale of the CCD (in arcsec/pixel), $\mu(r)$ can be expressed in units of mag/arcsec². With the use of observed standard stars, the magnitudes and surface brightnesses can be transformed to a standard photometric system.

2.4 Global parameters

The surface photometry has produced radial profiles of a number of quantities. It is desirable to condense these radial profiles to a few characteristic numbers, the global parameters.

2.4.1 Effective parameters

Elliptical galaxies have surface brightness profiles that are well approximated by the $r^{1/4}$ law (de Vaucouleurs 1948). By fitting the aperture magnitudes to an $r^{1/4}$ growth curve, the following two parameters can be derived:

- r_e : Effective radius, in arcsec
- $\langle\mu\rangle_e$: Mean surface brightness within r_e , in mag/arcsec²

The seeing needs to be taken into account (Saglia et al. 1993).

For galaxies with perfect $r^{1/4}$ profiles, the effective radius r_e is the *half-light* radius, i.e. the radius that encloses half of the light from the galaxy. Spiral galaxies are better described by an exponential surface brightness profile than by an $r^{1/4}$ profile.

We can express the mean surface brightness in units of L_{\odot}/pc^2 , where L_{\odot} is the luminosity of the Sun in the given passband (e.g. Gunn r). We will call this quantity $\langle I \rangle_e$. The relation is

$\log\langle I \rangle_e = -0.4(\langle \mu \rangle_e - k)$, where the constant k is given by $k = M_\odot + 5 \log(206265 \text{ pc}/10 \text{ pc})$. As is seen, the calculation does not involve the distance to the galaxy, but only the absolute magnitude of the Sun in the given passband. The calculation of r_e in kpc from r_e in arcsec, however, does involve the distance to the galaxy.

With r_e as the half-light radius, it follows that the total luminosity is given by $L = 2\pi\langle I \rangle_e r_e^2$.

2.4.2 Global Fourier parameters

As is seen from Figure 8, also the Fourier parameters vary with radius. One way of getting a characteristic value of e.g. the $c_4(r)$ profile is to take the extremum value. In case the profile does not have a clear extremum, we can take the value at the effective radius. We will use the symbol c_4 for this characteristic value of $c_4(r)$.

Another way to get a global Fourier coefficient is to calculate an intensity weighted mean value as

$$\langle s_n \rangle \equiv \frac{\int_{r_{\min}}^{r_{\max}} I(r) \cdot s_n(r) dr}{\int_{r_{\min}}^{r_{\max}} I(r) dr}, \quad \langle c_n \rangle \equiv \frac{\int_{r_{\min}}^{r_{\max}} I(r) \cdot c_n(r) dr}{\int_{r_{\min}}^{r_{\max}} I(r) dr}, \quad (11)$$

where r_{\min} is the radius where seeing effects are no longer important, and r_{\max} is the radius where the Fourier coefficients can no longer reliably be determined (see Jørgensen & Franx 1994).

2.4.3 Global ellipticities and colors

As global ellipticity can be taken the extremum of the $\epsilon(r)$ profile, the value of $\epsilon(r)$ at the effective radius, or the value of $\epsilon(r)$ at a certain isophote level, e.g. $\mu = 21.85^m/\text{arcsec}^2$ in Gunn r as used by Jørgensen & Franx (1994).

As global color, the color within the effective radius can be used. By color is meant the difference between the magnitudes in two different passbands, such as (B–V). The color is always calculated as the magnitude in the passband with the shortest effective wavelength minus the magnitude in the passband with the longest effective wavelength. Thus, a large value of the color means that the galaxy is red, and a small value means that it is blue. Another global parameter related to the color is the color gradient, defined as $\Delta\text{color}/\Delta \log r$, i.e. as the slope of the color versus $\log r$ plot.

3. QUANTITATIVE MORPHOLOGY FOR E AND S0 GALAXIES

CCD surface photometry as described in the previous section offers the possibility of carrying out quantitative morphologic studies of E and S0 galaxies. The traditional classification of these galaxies distinguishes between E and S0 galaxies based on the presense of a disk (S0 galaxies) or no disk (E galaxies). E and S0 galaxies are considered to belong to two separate classes of galaxies.

In the following we summarize the methods and results presented by Jørgensen & Franx (1994, hereafter JF94). The results lead to the conclusion that E and S0 galaxies fainter than an absolute blue magnitude of $M_{B_T} = -22$ mag form one class of galaxies with a broad and continuous distribution of the relative luminosity of the disks.

3.1. Sample properties and the data

The sample used in the study by JF94 is a magnitude limited sample of galaxies within the central square degree of the Coma cluster. The sample is complete to an apparent magnitude in Gunn r of 15.3 mag. 171 galaxies are included in the sample. Because the sample is well-defined and complete it is possible based on these data to draw conclusions regarding the E and S0 galaxies as a class.

CCD photometry was obtained of the full sample. Surface photometry for the galaxies was derived using GALPHOT (Jørgensen et al. 1992; Franx et al. 1989b). From the surface photometry, global parameters were derived. The important parameters used in this study are summarized in Table 4. $\langle c_4 \rangle$ and $\langle c_6 \rangle$ are intensity weighted mean values of c_4 and c_6 , respectively (see JF94 and Section 2.4.2), while c_4 represents the extremum the c_4 radial profile. The intensity weighted parameters are less sensitive to small scale features in the radial profiles and are therefore to be preferred for studies of global properties.

3.2. Morphology of the E and S0 galaxies

Figure 9 shows the morphological parameters $\epsilon_{21.85}$, $\langle c_4 \rangle$ and $\langle c_6 \rangle$ as functions of the total magnitudes m_T in Gunn r . The spiral galaxies are also shown on these figures, but we will omit them from the following discussion. From Figure 9 it is clear that the galaxies fainter than about 12.7 mag span the full range in morphological parame-

Table 4. Surface photometry parameters

Parameter	Description
m_T	Total magnitude in Gunn r
$\epsilon_{21.85}$	Ellipticity at $\mu = 21.85^m/\text{arcsec}^2$ in Gunn r
c_4	Extremum of the $c_4(r)$ radial profile
$\langle c_4 \rangle$	Intensity weighted mean value of $c_4(r)$
$\langle c_6 \rangle$	Intensity weighted mean value of $c_6(r)$

ters. The E and S0 galaxies cannot be separated into two classes of galaxies based on one of these morphological parameters. The difference in properties of E and S0 galaxies fainter and brighter than $m_T = 12.7$ mag is striking. This demarcation magnitude corresponds to a blue absolute magnitude of $M_{B-T} = -22$ mag.

In Figure 10 we show the distribution of the ellipticities, $\epsilon_{21.85}$, of the galaxies. Figure 10b shows the cumulative frequency of $\epsilon_{21.85}$ for the E galaxies and the S0 galaxies separately, as well as the cumulative frequency of $\epsilon_{21.85}$ for the E and S0 galaxies as one class.

If the E galaxies and the S0 galaxies form two separate classes, then we expect that their $\epsilon_{21.85}$ distributions can be modeled independently. The simplest assumption is that the galaxies are randomly oriented in space and have some simple distribution of the *intrinsic* ellipticities. JF94 attempted to fit the $\epsilon_{21.85}$ distributions with intrinsically uniform ellipticity distributions and with intrinsic ellipticity distribution that were Gaussians. The fit was done by maximizing the probability that the data was drawn from the model as reflected by a Kolmogorov–Smirnov (K–S) test (e.g. Press et al. 1992). The K–S test gives the probability that a data distribution is drawn from a model distribution (or another data distribution) based on the maximum difference between the cumulative frequencies of the two distributions, as it is illustrated in Figure 10b. JF94 found that the $\epsilon_{21.85}$ distribution of the E galaxies could be fitted satisfactory with either a uniform or a Gaussian intrinsic distribution of the ellipticities. Both of these models resulted in probabilities of 84 per cent or larger. However, the $\epsilon_{21.85}$ distribution of the S0 galaxies could not be fitted satisfactory. Both intrinsic distributions have probabilities of only 11 per cent. The $\epsilon_{21.85}$ distribution of the S0 galaxies lack apparently round galaxies, see Figure 10b. JF94 also find that the $\epsilon_{21.85}$ distribution of the E and S0 galaxies treated as

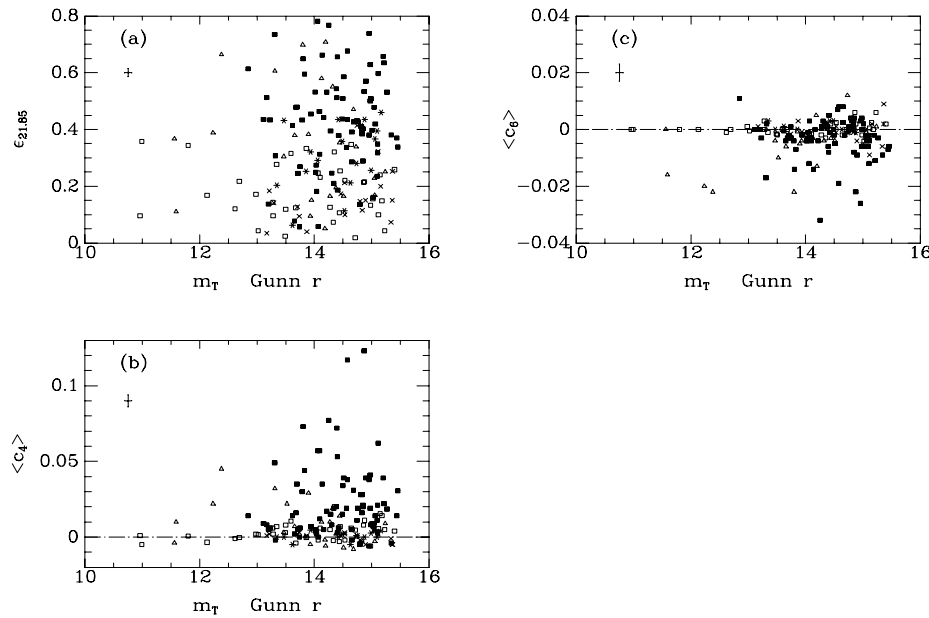


Fig. 9. Morphological parameters versus the total magnitudes. Open boxes – E galaxies with dominating regular c_4 -profiles; filled boxes – S0 galaxies with dominating regular c_4 -profiles; crosses – E galaxies with irregular or non-dominating c_4 -profiles; stars – S0 galaxies with irregular or non-dominating c_4 -profiles; triangles – spirals. The c_4 -profiles are considered non-dominating if $|\langle c_4 \rangle|$ is more than one sigma smaller than the absolute value of one of the other intensity weighted mean coefficients. Typical measurement errors are given on the panels. Galaxies with uncertainty on c_4 respectively $\langle c_4 \rangle$ larger than 0.02 are not plotted. The six brightest galaxies have small Fourier coefficients and $\epsilon_{21.85} < 0.4$. Other dependence on m_T is not seen. (From JF94.)

one class can be fitted satisfactory by either a uniform or a Gaussian intrinsic distribution of the ellipticities.

These results show that some (maybe all) of the E galaxies fainter than $m_T = 12.7$ mag must be S0 galaxies seen face-on. When the galaxies are seen face-on a disk is more difficult to detect (as also noted by Rix & White 1990), and the galaxies are mostly classified as E galaxies even when a disk is present.

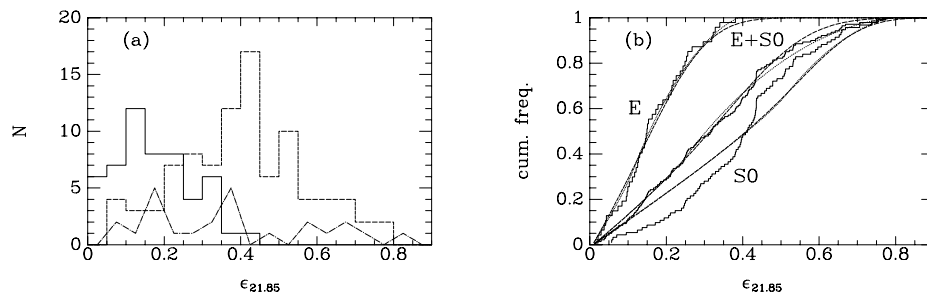


Fig. 10. Distributions of the apparent ellipticities. (a) Solid line – E galaxies, dashed line – S0 galaxies, Dashed-dotted line – spirals. (b) Solid lines – E, S0 galaxies, and E and S0 galaxies together. The six brightest E galaxies are excluded. Dotted lines – best fitting uniform distributions. Dashed lines – best fitting Gaussian distributions. (From JF94.)

3.3 The relative disk luminosities

The next task is to determine the relative disk luminosities, L_D/L_{tot} , of the galaxies. L_D/L_{tot} is the luminosity of the disk relative to the total luminosity of the galaxy. JF94 showed that two of the morphological parameters can be used together to derive L_D/L_{tot} if a simple model for the disk and the bulge is assumed.

Figure 11 illustrates this technique for the Coma cluster sample. JF94 constructed models consisting of a bulge with an $r^{1/4}$ profile and a disk with an exponential profile. The bulge is assumed to have an intrinsic ellipticity of 0.3, while the intrinsic ellipticity of the disk is assumed to be 0.85. JF94 tested models for both equal major axis of the two components, $a_{eB} = a_{eD}$, and for $a_{eB} = 0.5a_{eD}$. The results are not significantly different, so here we will concentrate on the $a_{eB} = a_{eD}$ models. JF94 convolved the model images of bulge plus disk with a representative seeing and then analyzed the model images in the same way as done for the data. Models with relative disk luminosities L_D/L_{tot} between zero (no disk) and one (all disk) were constructed. Further, the inclination was varied between face-on (small inclination, $\cos i = 1$) and edge-on (large inclination, $\cos i = 0$) in steps of 0.1 in $\cos i$.

The results in terms of morphological parameters are shown on Figure 11. The models reproduce the general variation of c_4 , $\langle c_4 \rangle$ and $\langle c_6 \rangle$ with ellipticity. They also span reasonably well the section of the $\langle c_4 \rangle$ – $\langle c_6 \rangle$ diagram covered by the data. Models of the kind used by

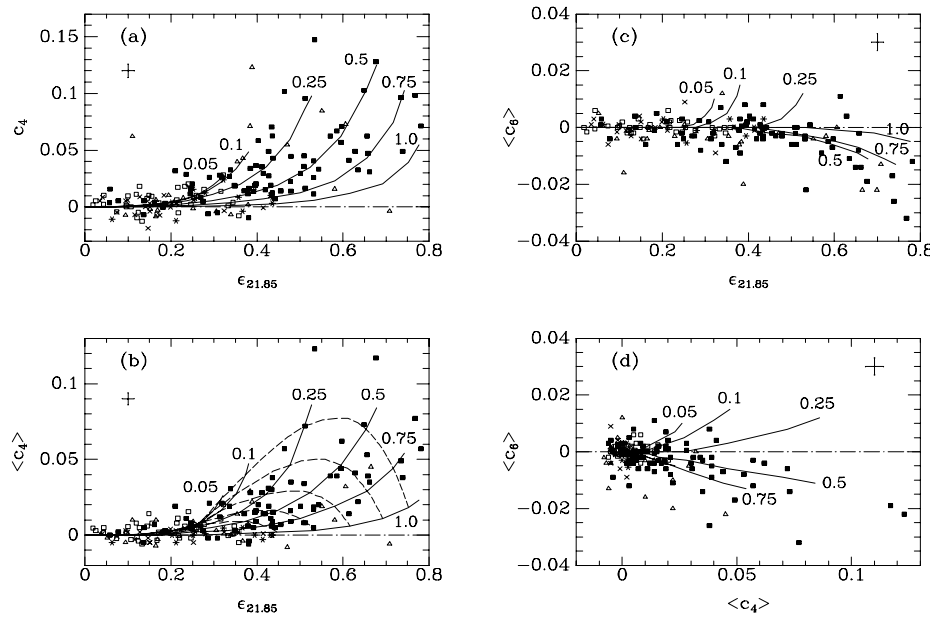


Fig. 11. Fourth and 6th order Fourier coefficients plotted against ellipticity and versus each other. Data symbols as in Figure 9. Galaxies with uncertainty on c_4 respectively $\langle c_4 \rangle$ larger than 0.02 are not plotted. Typical measurement errors are given on the panels. The models with $a_{\text{eB}} = a_{\text{eD}}$ are overplotted. The curves are labeled with L_D/L_{tot} . The dashed lines on (b) mark the inclinations where $\cos i = 0.1, 0.2, 0.3, 0.4$, and 0.5 (i.e. $i = 84^\circ, 78^\circ, 73^\circ, 66^\circ$, and 60°), from top to bottom. No dashed line is shown for the $i = 90^\circ$ (i.e. edge-on) models, but this line would be above the $i = 84^\circ$ dashed line, connecting the end points of the solid lines. It is seen that for a given L_D/L_{tot} the highest inclination gives the largest $\langle c_4 \rangle$. The non-zero coefficients for the pure disk-model are due to the inclusion of seeing effects in the models. (From JF94.)

JF94 cannot reproduce boxy isophotes of the galaxies. However, the Coma cluster sample contains only two galaxies fainter than $m_T = 12^{\text{m}}7$ that have $\langle c_4 \rangle$ significantly smaller than zero. For galaxies with ellipticities larger than 0.3 and $\langle c_4 \rangle$ larger than 0.007, the models are well separated in $\langle c_4 \rangle$ versus $\epsilon_{21.85}$, see Figure 11b. Thus, these two parameters can be used to derive the relative disk luminosities, L_D/L_{tot} , and the inclinations, i , of the galaxies.

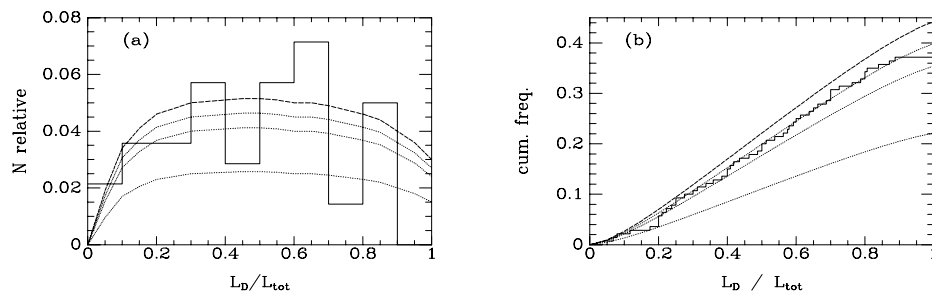


Fig. 12. Relative (a) and cumulative (b) frequency for the relative disk luminosities. Solid line – determinations from the $\epsilon_{21.85}-\langle c_4 \rangle$ diagram. The distribution has been normalized with the total number of galaxies fainter than $m_T = 12^m7$. Dashed line – model prediction for a uniform intrinsic distribution, corrected for the incompleteness due to the limits enforced on $\epsilon_{21.85}$ and $\langle c_4 \rangle$. Dotted lines – model predictions for a uniform intrinsic distribution plus a fraction of diskless galaxies. Models for fractions of 0.1, 0.2, and 0.5 are shown. A higher fraction of diskless galaxies moves the curve for the normalized distribution downwards in both (a) and (b). (From JF94.)

Figure 12 shows the resulting distribution of L_D/L_{tot} . It was possible to derive L_D/L_{tot} for 52 of the E and S0 galaxies in the sample. The cumulative frequency shown on Figure 12b is normalized to the 140 E and S0 galaxies fainter than $m_T = 12.7$ mag. Overplotted on Figure 12 are models of the distribution of L_D/L_{tot} . These models are uniform distributions with some fraction of diskless galaxies added. The best fitting model is a uniform distribution of L_D/L_{tot} between zero and one with an additional 10 per cent diskless galaxies. JF94 find that the resulting distributions of inclinations, $\epsilon_{21.85}$ and $\langle c_4 \rangle$ for this model also fit the observed distributions of these parameters.

3.4 Conclusions from JF94

The results presented by JF94 illustrate the strengths of studies of quantitative morphology based on surface photometry for statistically well-defined and complete samples. JF94 were able to show that the E and S0 galaxies in the Coma cluster (fainter than $m_T = 12.7$ mag in Gunn r) form one class of galaxies with a broad (most likely uniform) distribution of L_D/L_{tot} . This result contradicts the tra-

ditional classification of these galaxies into two separate classes. It also provides constraints for models for morphological evolution of galaxies, since the end-result for the Coma cluster represents one scenario that the models need to reproduce.

4. STELLAR POPULATION MODELS

Stellar population models are tools for interpreting the integrated light, such as the colors, observed from galaxies. Ideally, we want to determine the mix of stars that give rise to the observations. This problem is usually underconstrained, so it is necessary to make some assumptions regarding how the numbers of different types of stars are related. Here we will consider so-called single-age single-metallicity models, also known as single stellar population (SSP) models. In these models, all the stars are formed at the same time, with distribution in mass given by the chosen initial mass function (IMF), and with identical chemical composition.

SSP models are based on the following ingredients. First, theoretical stellar isochrones are needed. Isochrones are loci in the theoretical HR-diagram ($\log T_{\text{eff}}$, $\log L$) for a stellar population of a given age and chemical composition. Second, a conversion is needed between the theoretical parameters of T_{eff} , L , $\log g$ (surface gravity) and the metallicity $[M/H]$ to the observable parameters such as colors. This conversion can be either empirical or theoretical. The empirical conversion is based on observations of individual stars in our Galaxy for which the ‘theoretical parameters’ can be inferred, and the observable parameters measured. The theoretical conversion is based on model atmospheres and synthetic spectra. Third, the IMF has to be specified.

An example of SSP models are those presented by Vazdekis et al. (1996). These models use the isochrones from the Padova group (Bertelli et al. 1994). The conversion from the theoretical to the observable parameters is empirical. Models are presented for several different IMFs. One IMF is a constant below $0.2 M_{\odot}$, a Salpeter (1955) IMF above $0.6 M_{\odot}$, and a spline in the interval $0.2\text{--}0.6 M_{\odot}$. The models that we use in Section 5 are based on this IMF.

When the IMF has been specified, the models have only two parameters: age and metallicity. The metallicity can be expressed either as the mass fraction in heavier elements, Z , or as the metal

abundance $[M/H] \equiv \log(Z/Z_{\odot})$ (with $Z_{\odot} = 0.02$). The models have solar abundance ratios, while this may not be the case for all galaxies.

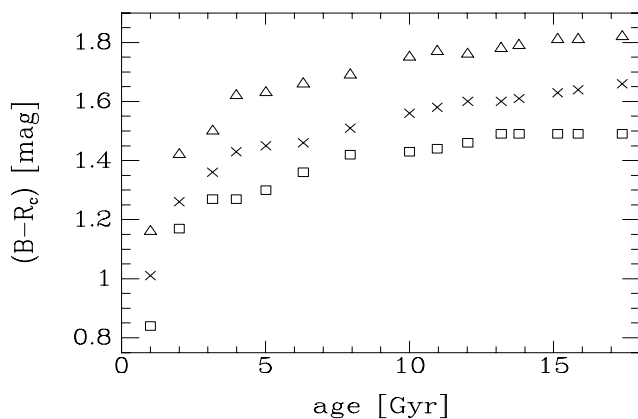


Fig. 13. Example of the predictions from the Vazdekis et al. (1996) models: $(B-R_c)$ color as function of age (the x -axis) and metallicity (the different symbols). Triangles – $[M/H] = 0.4$; crosses – $[M/H] = 0.0$; boxes – $[M/H] = -0.4$. It is seen that the stellar populations get redder with higher age and higher metallicity.

As an example, the model predictions for the $(B-R_c)$ color is given in Figure 13. It is seen that the color depends both on age and metallicity. As will be illustrated in the next section, optical colors depend roughly in the same way on age and metallicity. Therefore, in a plot of one optical color versus another optical color the model lines of constant age will be almost on top of the model lines of constant metallicity. The effects of age and metallicity cannot be disentangled in such a diagram. This is known as the *age–metallicity degeneracy* (e.g. Worthey 1994).

It should be noted that real galaxies are not necessarily single stellar populations. For example, a galaxy could have experienced a second star formation event. Therefore, when SSP model predictions are compared with data for real galaxies to determine the age and the metallicity, the resulting ages and metallicities are luminosity weighted mean values. Further, dust can also cause a stellar population to appear red. This can be an additional complication in determining ages and metallicities.

5. COLOR RELATIONS

The E and S0 galaxies follow very well-defined relations between the optical colors and the total magnitudes. Figure 14 shows the optical color-magnitude relation for the Coma cluster. The figure includes all objects detected in a field covering the central $75 \text{ arcmin} \times 80 \text{ arcmin}$ of the cluster. The data were obtained with the McDonald Observatory 0.8-meter Telescope equipped with the Prime Focus Camera.

The color-magnitude relation is well-defined and has a very low scatter for (E and S0) galaxies brighter than about $R_c = 17 \text{ mag}$, see Figure 14. For galaxies fainter than $R_c = 17.5 \text{ mag}$ only sparse redshift information is available, and many of these faint galaxies may be background galaxies.

The color-magnitude relation is thought to be primarily a result of differences in metallicity as a function of luminosity. However, recent results based on spectroscopy show that both the mean ages and the mean metallicities varies for E and S0 galaxies at low redshifts (e.g. Worthey, Trager & Faber 1995; Jørgensen 1999). Thus, there is a need for interpreting the color-magnitude relation within these recent results in order to achieve a self-consistent interpretation of the spectroscopic and the photometric results. The work by Kauffmann & Charlot (1998) represents one of the only attempts to model the color-magnitude relation and relations involving spectroscopic information in a consistent manner. In the models by Kauffmann & Charlot both age and metallicity varies with the luminosity.

Color-color relations in the optical are in Figure 15 shown for the same sample of objects as shown in Figure 14. The confirmed members of the cluster form a tight relation in these two color-color relations. This is in agreement with predictions from stellar population models (see Section 4), which predicts the optical colors to be degenerate in age and metallicity. This is seen on Figure 15, left panel, where the same models as shown on Figure 13 are overplotted. The lines of constant age fall right on top of the lines of constant metallicity, forming a single line along the ridge of the location of the E and S0 galaxies. This means that the optical colors alone cannot be used to derive the mean ages and the mean metallicities. A younger age will lead to bluer colors, but a similar change in colors can be caused by a lower metallicity.

While the optical color-color diagrams are degenerate in age and metallicity, the combination of one optical color and one optical-

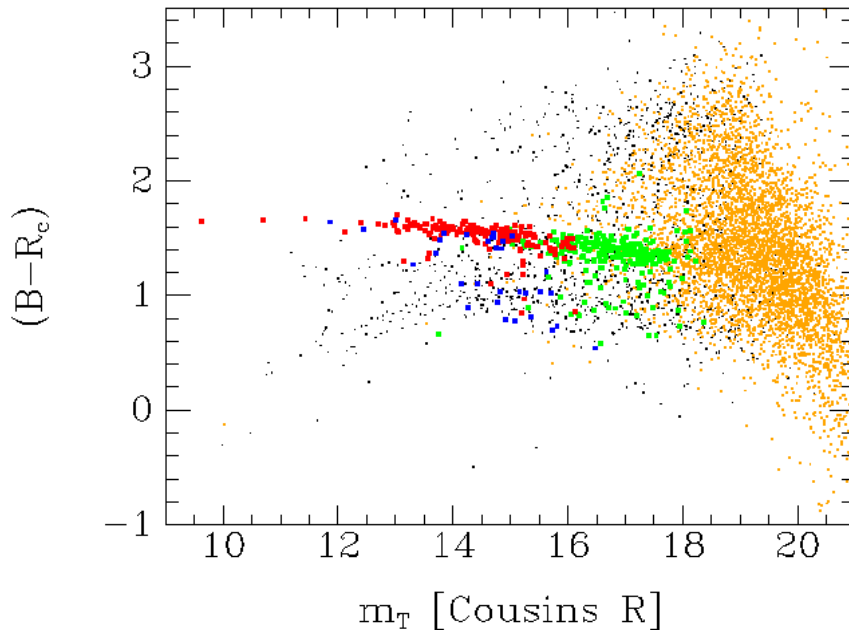


Fig. 14. Color-magnitude relation for the central $75 \text{ arcmin} \times 80 \text{ arcmin}$ of the Coma cluster. Both stars and galaxies are included on this figure, a total of 15370 objects. The lack of objects in the upper right hand corner is due to the combination of the magnitude limits in B and R_c . Small black points – stars; black [blue] boxes – spirals and irregulars, confirmed members; dark grey [red] boxes – E and S0 galaxies, confirmed members; light grey [green] boxes – unclassified confirmed members; small grey [orange] points – other galaxies in the field, members and non-members. The photometric data are from Jørgensen (2000). The redshift data are from Jørgensen & Hill (2000).

infrared color may be used to break the degeneracy. An example of this is shown in Figure 16 for a small sample of E and S0 galaxies in the Coma cluster. The optical color ($U-B$) and the optical-infrared color ($V-K$) are both sensitive to both age differences and metallicity differences. However, ($U-B$) is more sensitive to the age differences than to metallicity differences, while the opposite is the case for ($V-K$). The stellar population models in the near infrared (near-IR), JHK, in this case the K-band, are still rather uncertain, but

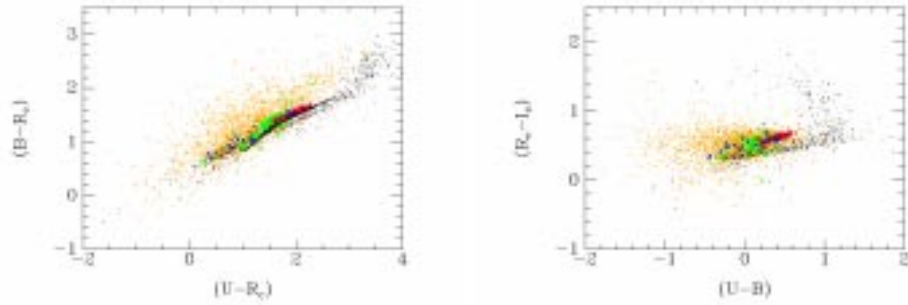


Fig. 15. Optical color-color relations for the Coma cluster. Symbols as in Figure 14. Solid line on the left panel – SPP models from Vazdekis et al. (1996), see text.

the technique is promising for studies of faint high redshift galaxies for which spectroscopy would come at a very high cost of telescope time at 8-meter class telescopes. The apparently rather low mean age of the Coma cluster galaxies as estimated from Figure 16 is in fact in agreement with results based on spectroscopic information (see Jørgensen 1999).

6. THE FUNDAMENTAL PLANE

The Fundamental Plane (FP) is a relation that combines surface photometry with spectroscopy. We will discuss this relation both at low and at high redshift.

The FP (Djorgovski & Davis 1987; Dressler et al. 1987) is the relation

$$\log r_e = \alpha \log \sigma + \beta \log \langle I \rangle_e + \gamma , \quad (12)$$

where σ is the line-of-sight stellar velocity dispersion for the galaxy in question. In other words, the measured values of $\log r_e$, $\log \langle I \rangle_e$ and $\log \sigma$ for a sample of E and S0 galaxies do not populate this 3-parameter space evenly, but are limited to a thin plane.

The velocity dispersion σ is determined from spectroscopy, see Figure 17. The absorption lines in galaxies are broadened due to the internal motions of the stars in the galaxy. To determine how much the stars are moving, it is necessary to know what the spectrum of the galaxy would be if all the stars were at rest with respect to each other. This is approximated by the spectrum of a K giant star. This

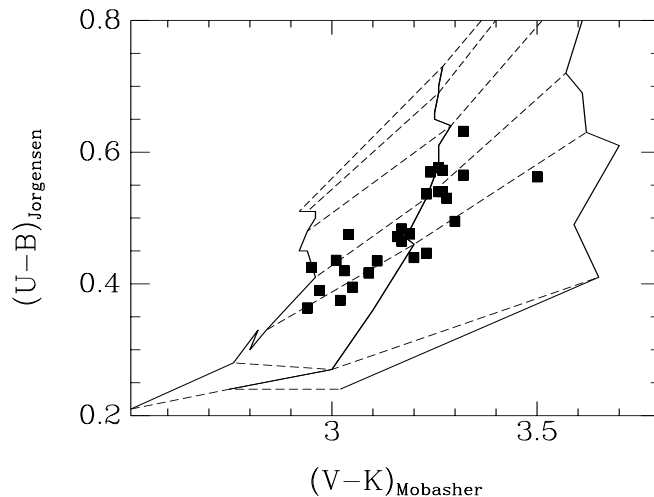


Fig. 16. Optical-infrared color-color relation for the Coma cluster. The data are from Jørgensen (2000) and Mobasher et al. (1999). The lines represent stellar population models by Vazdekis et al. (1996). Solid lines – metallicities of $[\text{Fe}/\text{H}] = -0.4, 0.0$ and 0.4 ; the lowest metallicity leads to the smallest $(V-K)$. Dashed lines – ages of 1, 2, 5, 8, 12, 15, and 17 Gyr; the largest ages lead to the largest $(U-B)$.

template star spectrum is broadened by a Gaussian broadening function until it matches the galaxy spectrum. The velocity dispersion of the galaxy is then the dispersion σ of the broadening function. In more precise terms, this determination of σ can be done using the Fourier fitting method (Franx, Illingworth & Heckman 1989a) or the Fourier quotient method (Sargent et al. 1977).

6.1 The interpretation of the Fundamental Plane

The physics behind the FP can be illuminated by some simple arguments (Djorgovski, de Carvalho & Han 1988; Faber et al. 1987). Consider the virial theorem for the stars in the galaxy

$$\frac{GM}{\langle R \rangle} = 2 \frac{\langle V^2 \rangle}{2}, \quad (13)$$

We relate the observable quantities r_e , σ and $\langle I \rangle_e$ to the ‘physical’ quantities $\langle R \rangle$, $\langle V^2 \rangle$ and luminosity L through

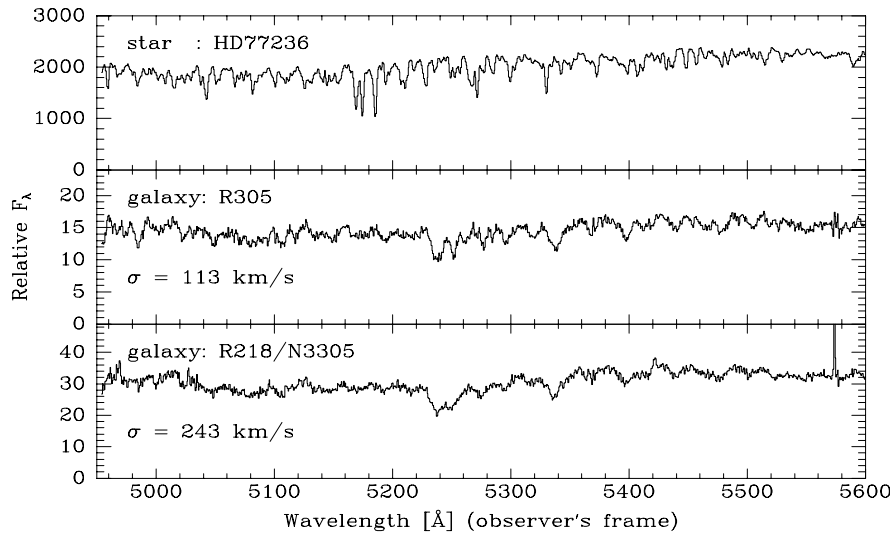


Fig. 17. Illustration of the effect of the velocity dispersion σ . The top panel shows a K giant star in our own Galaxy. This star is representative of the stellar populations in E or S0 galaxies. The two lower panels show E or S0 galaxies in the HydraI cluster. The Mg b absorption line triplet at 5177 Å (rest frame) is broadened in the galaxy spectra. The instrumental resolution is 79 km/s.

$$r_e = k_R \langle R \rangle, \quad \sigma^2 = k_V \langle V^2 \rangle, \quad L = k_L \langle I \rangle_e r_e^2, \quad (14)$$

The parameters k_R , k_V , and k_L reflect the density structure, kinematical structure, and luminosity structure of the given galaxy. If these parameters are constant, the galaxies constitute a *homologous* family. Homology means that structure of small and big galaxies is the same.

Combining Equation (13) and (14) gives

$$r_e = k_S (M/L)^{-1} \sigma^2 \langle I \rangle_e^{-1}, \quad k_S = (G k_R k_V k_L)^{-1}. \quad (15)$$

For homology k_S will be constant. When this relation is compared to the observed FP,

$$r_e = \text{constant} \cdot \sigma^{1.24 \pm 0.07} \langle I \rangle_e^{-0.82 \pm 0.02} \quad (16)$$

(Jørgensen, Franx & Kjaergaard 1996, in Gunn r), it is seen that the coefficients of the FP are not 2 and -1 as expected from homology and constant mass-to-light ratios. The product $k_S (M/L)^{-1}$ cannot

be constant, but has to be a function of σ and $\langle I \rangle_e$. A non-constant $k_S(M/L)^{-1}$ can be explained by a systematic deviation from homology (k_S varies), or a systematic variation of the M/L ratios, or both. When homology is assumed, the observed FP coefficients give the relation

$$M/L_r \propto M^{0.24 \pm 0.03}, \quad (17)$$

(Jørgensen et al. 1996). The interpretation of the FP is still a matter of debate. The $M/L \propto M^b$ interpretation seems to be the most favored one, although there is some evidence that non-homology may play a role too (e.g. Hjorth & Madsen 1995; Pahre, de Carvalho & Djorgovski 1998).

6.2 The evolution of the Fundamental Plane as a function of redshift

The Fundamental Plane can be used to study the evolution of galaxies as a function of redshift. As explained above, the FP may be interpreted as a relation between the masses and the M/L ratios of the galaxies. Under the assumption that the masses do not change with redshift, e.g. no merging takes place, the evolution of the FP zero point with redshift can be interpreted as the evolution of the M/L ratios.

Several authors have studied the FP for clusters at redshifts higher than 0.1, see Table 5 for clusters and references. Additional studies by Pahre, Djorgovski & de Carvalho (1999) and Kelson et al. (1999) are soon to be published in refereed journals.

Table 5. Fundamental Plane studies of cluster with $z > 0.1$

Cluster	z	N_{gal}	Reference
A2218	0.18	9	Jørgensen & Hjorth (1997), Jørgensen et al. (1999)
A665	0.18	6	Jørgensen & Hjorth (1997), Jørgensen et al. (1999)
CL1358+62	0.33	10	Kelson et al. (1997)
MS1512+36	0.37	2	Bender et al. (1998)
A370	0.37	7	Bender et al. (1998)
CL0024+16	0.39	8	van Dokkum & Franx (1996)
MS2053−04	0.58	5	Kelson et al. (1997)
MS1054−03	0.83	8	van Dokkum et al. (1998)

As examples of high redshift studies of the FP we show in Figure 18 the FP for the Coma cluster and for five clusters with redshift larger than 0.1. The data for the Coma are from Jørgensen (1999) and Jørgensen et al. (1995). Abell 2218 and Abell 665 are discussed by Jørgensen et al. (1999). The sources for the rest of the clusters are given on the figure.

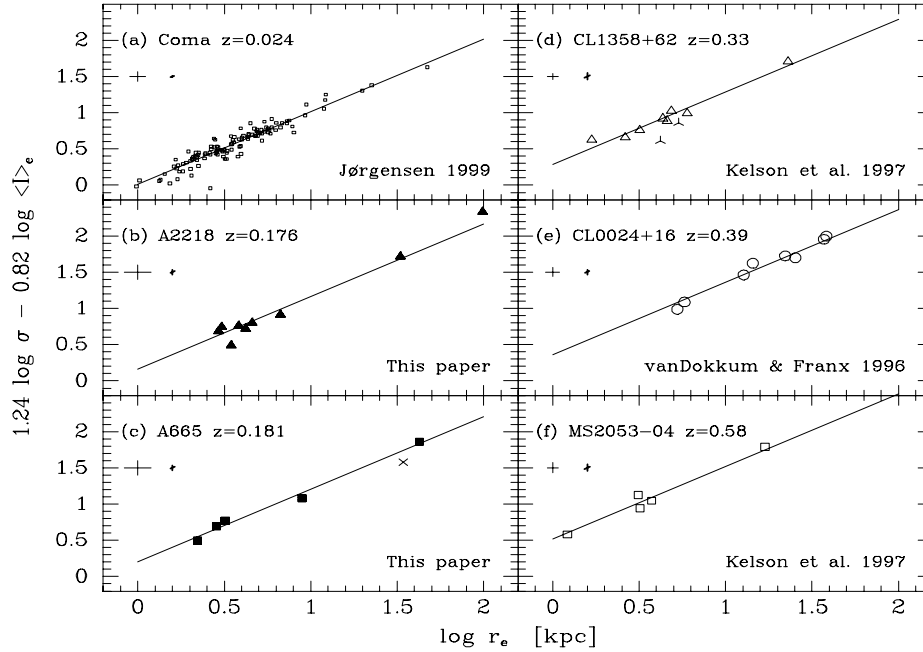


Fig. 18. The FP edge-on for Coma, A2218, A665, CL1358+62, CL0024+16, and MS2053-04. The sources of the data are given on the panels ('This paper' refers to Jørgensen et al. 1999). The skeletal symbols on panel (c) and (d) are the E+A galaxies. The photometry is calibrated to Gunn r in the rest frames of the clusters. The mean surface brightness $\log \langle I \rangle_e = -0.4(\langle \mu \rangle_e - 26.4)$ is in units of L_\odot/pc^2 (cf. Section 2.4.1). The photometry is not corrected for the dimming due to the expansion of the Universe. The effective radii are in kpc ($H_0 = 50 \text{ km s}^{-1} \text{ Mpc}^{-1}$ and $q_0 = 0.5$). The solid lines are the FPs with coefficients adopted from Jørgensen et al. (1996), and with zero points derived from the data presented in the figure. Typical error bars are given on the panels; the thin and thick error bars show the random and systematic uncertainties, respectively. (From Jørgensen et al. 1999.)

From the change in the zero point of the FP as a function of redshift Jørgensen et al. (1999), in agreement with other studies, find that the M/L ratios of the E and S0 galaxies change very slowly with redshift. The sample of clusters shown on Figure 18 span about half of the current age of the Universe (for $q_0 = 0.5$). Under the assumption that the galaxies evolve passively over this time interval, e.g. no merging and no formation of new E and S0 galaxies, then it is possible to put limits of the redshift at which the majority of the stars were formed. This redshift is called the formation redshift. The study by Jørgensen et al. (1999) as well as other studies conclude that the formation redshift is larger than about 2.5 for $q_0 = 0.5$ and larger than about 1.5 for $q_0 = 0.15$.

It is important to keep in mind that the assumption regarding passive evolution represents a very simplified view of the galaxy evolution. Most likely the real evolution since $z \approx 0.6$ cannot be modeled with passive evolution. If the galaxies experience on-going star formation, then the observed evolution will appear smaller than for passive evolution because the galaxies are continuously forming young bright stars. A similar effect can be caused by a series of smaller bursts of star formation. Finally, the interactions, the possible merging and the morphological evolution of the galaxies over the last half of the age of the Universe cannot be ignored. Some of the E and S0 galaxies that we observe in low redshift clusters may not have ended up in the samples if we could have observed those clusters at a much earlier stage in their evolution, simply because some of the E and S0 galaxies may have formed recently by merging of spiral galaxies.

7. SUGGESTED FUTURE PROJECTS

We end this paper by a brief summary of some of the projects that may be carried out building on the techniques and results discussed in this paper. We concentrate on projects that involve photometry only. Some of the projects may be carried out using existing archive data from HST.

Evolution of morphology as a function of redshift

Dressler et al. (1997) have recently used HST/WFPC2 data of clusters to study the morphology-density relation as a function of

redshift. Dressler et al. found that the fraction of S0 galaxies is lower at high redshift than at low redshift, while the fraction of spirals is higher at high redshift than at low redshift. However, this study is based on the traditional method of classifying galaxies. We suggest that a quantitative approach is taken to any study of the morphology. Of special interest would be to study how the relative disk luminosities L_D/L_{tot} for E and S0 galaxies evolve with redshift, both in clusters and in the field. The first study of this kind was done for the cluster CL0024+16 ($z = 0.39$) by Bergmann & Jørgensen (1999) who found that the L_D/L_{tot} distribution for the E and S0 galaxies in CL0024+16 shows a paucity of disk-dominated galaxies when compared to the Coma cluster.

It would be valuable to apply the same technique and derive L_D/L_{tot} for a larger sample of cluster and field galaxies at redshifts larger than 0.1 to establish the possible evolution of the distribution of L_D/L_{tot} . This may be done using the HST/WFPC2 archive data.

Studies of global colors

There have been many studies of the global colors of galaxies as a function of redshift (e.g. Stanford, Eisenhardt & Dickinson 1998; Bower, Kodama & Terlevich 1998; Kodama et al. 1998 and references in these papers). However, most studies concentrate on the optical colors of the galaxies, while the near-IR (JHK) data is very sparse. The study by Stanford et al. includes near-IR data and addresses the question of how the color-magnitude relations for the near-IR colors evolve with redshift.

The combination of optical and optical-infrared colors may be used to break the age-metallicity degeneracy (see Section 5). Observations of low redshift E and S0 galaxies in the near-IR may be used to establish the zero redshift properties and the methods and models needed to break the age-metallicity degeneracy. For high redshift galaxies ($z > 0.5$), the near-IR photometry may be obtained with 8-meter class telescopes with superior spatial resolution. Such data will give the possibility of studying the mean ages and mean metallicities as functions of redshift for significantly fainter galaxies than it is currently possible by obtaining spectroscopy with 8-meter class telescopes.

Color gradients

While we have not discussed color gradients in this paper, color gradients provide an alternative method of studying galaxy evolution. The color gradients in E and S0 galaxies reflect underlying radial gradients in the metallicity (and maybe the age) of the stellar populations. Models for galaxy formation predict the sizes of these gradients. In general, the predicted gradients are steeper for models based on a monolithic collapse (Carlberg 1984) than for models based on the merger hypothesis (White 1980). Determination of color gradients for high redshift galaxies requires high signal-to-noise data with very good spatial resolution. Several of the rich galaxy clusters observed with HST/WFPC2 have sufficiently high signal-to-noise data that a study may be carried out using the available archive data.

ACKNOWLEDGEMENTS. It is a pleasure to thank the organizers for a successful and stimulating school. Support from the Nordic Research Academy (REF 99.10.003-B) for the course is kindly acknowledged, as well as support from Nato Scientific and Environmental affairs division linkage grant, Computer network supplement 97 46622 Re CRG.LG 972172 for the Internet connection.

The data used in this paper were obtained at the Nordic Optical Telescope, the Danish 1.5-meter Telescope LaSilla, the Kitt Peak National Observatory 4-meter Telescope, the Multi-Mirror Telescope, the McDonald Observatory 0.8-meter and 2.7-meter Telescopes, and the Hubble Space Telescope. We thank the telescope allocation committees for granting time to these project, and the staff at NOT, ESO/LaSilla, KPNO, MMT and McDonald Observatory for assistance during the observations.

REFERENCES

- Abraham R. G., Valdes F., Yee H. K. C., van den Bergh S., 1994, *ApJ*, 432, 75
Abraham R. G., van den Bergh S., Glazebrook K., Ellis R. S., Santiago B. X., Surma P., Griffiths R. E., 1996, *ApJS*, 107, 1
Bender R., Möllenhoff C., 1987, *A&A*, 177, 71
Bender R., Döbereiner S., Möllenhoff C., 1988, *A&AS*, 74, 385
Bender R., Saglia R. P., Ziegler B., Belloni R., Greggio L., Hopp U., Bruzual G., 1998, *ApJ*, 493, 529

- Bender R., Surma P., Döbereiner S., Möllenhoff C., Madejsky R., 1989, *A&A*, 217, 35
- Bergmann M., Jørgensen I., 1999, in *Galaxy Dynamics*, ASP Conference Series Vol. 182, eds. D. R. Merritt, M. Valluri, J. A. Sellwood, p. 505
- Bertelli G., Bressan A., Chiosi C., Fagotto F., Nasi E., 1994, *A&AS*, 106, 275
- Bower R. G., Kodama T., Terlevich A., 1998, *MNRAS*, 299, 1193
- Busko I., 1996, in *Astronomical Data Analysis Software and Systems V*, ASP Conference Series Vol. 101, eds. G. H. Jacoby, J. Barnes, p. 139
- Carlberg R. G., 1984, *ApJ*, 286, 403
- Carter D. 1987, *ApJ*, 312, 514
- Cawson M. C., 1983, PhD Thesis, University of Cambridge
- Davis L. E., Cawson M., Davies R. L., Illingworth G., 1985, *AJ*, 90, 169
- de Vaucouleurs G., 1948, *Ann. d'Ap.*, 11, 247
- Djorgovski S., Davis M., 1987, *ApJ*, 313, 59
- Djorgovski S., de Carvalho R., Han M.-S., 1988, in *The Extragalactic Distance Scale*, ASP Conference Series Vol. 4, eds. van den Bergh S., Prichet C. J., p. 329
- Dressler A., Lynden-Bell D., Burstein D., Davies R. L., Faber S. M., Terlevich R. J., Wegner G., 1987, *ApJ*, 313, 42
- Dressler A., Oemler A. Jr., Couch W. J., Smail I., Ellis R. S., Barger A., Butcher H., Poggianti B. M., Sharples R. M., 1997, *ApJ*, 490, 577
- Faber S. M., Dressler A., Davies R. L., Burstein D., Lynden-Bell D., Terlevich R. J., Wegner G., 1987, in *Nearly Normal Galaxies*, ed. Faber S. M. Springer, New York, p. 175
- Faber S. M., Tremaine S., Ajhar E. A., Byun Y.-I., Dressler A., Gebhardt K., Grillmair C., Kormendy J., Lauer T. R., Richstone D., 1997, *AJ*, 114, 177
- Franx M., Illingworth G., Heckman T., 1989a, *ApJ*, 344, 613
- Franx M., Illingworth G., Heckman T., 1989b, *AJ*, 98, 538
- Hjorth J., Madsen J., 1995, *ApJ*, 445, 55
- Jedrzejewski R. I., 1987, *MNRAS*, 226, 747
- Jørgensen I., 1999, *MNRAS*, 306, 607
- Jørgensen I., 2000, in preparation
- Jørgensen I., Franx M., 1994, *ApJ*, 433, 553 (JF94)
- Jørgensen I., Hill G., 2000, in preparation
- Jørgensen I., Hjorth J., 1997, in *Galaxy Scaling Relations: Origins, Evolution and Applications*, eds. L. N. da Costa, A. Renzini, Springer-Verlag, p. 175
- Jørgensen I., Franx M., Hjorth J., van Dokkum P., 1999, *MNRAS*, 308, 833

- Jørgensen I., Franx M., Kjaergaard P., 1992, *A&AS*, 95, 489
- Jørgensen I., Franx M., Kjaergaard P., 1995, *MNRAS*, 273, 1097
- Jørgensen I., Franx M., Kjaergaard P., 1996, *MNRAS*, 280, 167
- Kauffmann G., Charlot S., 1998, *MNRAS*, 294, 705
- Kelson D. D., van Dokkum P. G., Franx M., Illingworth G. D., Fabricant D., 1997, *ApJ*, 478, L13
- Kelson D. D., Illingworth G. D., Franx M., van Dokkum P. G., 1999, in *The High Redshift Universe: Galaxy Formation and Evolution at High Redshift*, ASP Conference Series, in press
- Kodama T., Arimoto N., Barger A. J., Aragón-Salamanca A., 1998, *A&A*, 334, 99
- Kormendy J., Djorgovski S., 1989, *ARA&A*, 27, 235
- Milvang-Jensen B., Jørgensen I., 2000, in preparation
- Mobasher B., Guzmán R., Aragón-Salamanca A., Zepf S., 1999, *MNRAS*, 304, 225
- Naim A., Lahav O., Sodre L. Jr., Storrie-Lombardi M. C., 1995, *MNRAS*, 275, 567
- Nieto J.-L., Bender R., 1989, *A&A*, 215, 266
- Okamura S., 1988, *PASP*, 100, 524
- Pahre M. A., de Carvalho R. R., Djorgovski S. G., 1998, *AJ*, 116, 1606
- Pahre M. A., Djorgovski S. G., de Carvalho R. R., 1999, in *Star Formation in Early Type Galaxies*, ASP Conference Series Vol. 163, eds. P. Carral, J. Cepa, p. 17
- Peletier R. F., Davies R. L., Illingworth G. D., Davis L. E., Cawson M., 1990, *AJ*, 100, 1091
- Press W. H., Teukolsky S. A., Vetterling W. T., Flannery B. P., 1992, *Numerical Recipes*, Cambridge University Press, New York
- Richter O.-G., 1989, *A&AS*, 77, 237
- Rix H.-W., White S. D. M., 1990, *ApJ*, 362, 52
- Saglia R. P., Bertschinger E., Baggle G., Burstein D., Colless M., Davies R. L., McMahan Jr. R. K., Wegner G., 1993, *MNRAS*, 264, 961
- Salpeter E. E., 1955, *ApJ*, 121, 161
- Sargent W. L. W., Schechter P. L., Boksenberg A., Shortridge K., 1977, *ApJ*, 212, 326
- Stanford S. A., Eisenhardt P. R., Dickinson M., 1998, *ApJ*, 492, 461
- Thuan T. X., Gunn J. E., 1976, *PASP*, 88, 543
- van Dokkum P. G., Franx M., 1996, *MNRAS*, 281, 985
- van Dokkum P. G., Franx M., Kelson D. D., Illingworth G. D., 1998, *ApJ*, 504, L17
- Vazdekis A., Casuso E., Peletier R. F., Beckman J. E., 1996, *ApJS*, 106, 307

White S. D. M., 1980, MNRAS, 191, 1p

Worthey G., 1994, ApJS, 95, 107

Worthey G., Trager S. C., Faber S., 1995, in Fresh Views on Elliptical Galaxies, ASP Conference Series Vol. 86, eds. A. Buzzoni, A. Renzini, A. Serrano, p. 203